Journal of the European Ceramic Society 19 (1999) 665–673

PII: S0955-2219(98)00294-5
0955-2219/99/$ - see front matter

# Structure and Composition of Grain Boundaries in Ceramics

F. Ernst, O. Kienzle and M. Rühle*

Max-Planck-Institut für Metallforschung, Seestraße 92, D-70174 Stuttgart, Germany

***Abstract***

*This paper reviews advanced techniques of transmission electron microscopy (TEM) to study the structure, composition, and charge distribution at interfaces in ceramics. Recent experimental studies on grain boundaries in lead titanate, silicon nitride, and strontium titanate serve as examples to demonstrate the advantages TEM in obtaining structural and chemical information at high spatial resolution. © 1999 Elsevier Science Limited. All rights reserved*

*Keywords*: grain boundaries, interfaces, electron microscopy, perovskites.

## 1 Introduction

Most materials of practical importance are used in polycrystalline form. This holds for ceramics (polycrystalline ceramic materials), metals, alloys, metal/ceramic or ceramic/ceramic composites, some polymers, and some advanced semiconductors. In polycrystalline materials, regions of different orientation and/or composition are separated from each other by internal interfaces. These 'internal' interfaces play an important and often dominant role in controlling materials properties. Several textbooks and proceedings of international conferences reflect the research activities in this area.[1–4] The importance of internal interfaces has become particularly obvious from the outstanding properties of nanocrystalline materials.[5] Understanding the properties of internal interfaces constitutes a challenge to materials science because interface properties depend on numerous parameters. The mere crystallography of a planar interface, for example, depends on up to ten different parameters: six macroscopic and four microscopic parameters.[2] The macroscopic parameters include (i) three parameters to describe the rotation of one crystal lattice with respect to the other, (ii) two parameters indicating the (average) inclination (or orientation) of the boundary plane, and, if either crystal displays enantiomorphism, (iii) one parameter to indicate whether the transformation from one crystal to the other requires an inversion or not. The microscopic degrees of freedom comprise (i) three parameters to indicate the 'translation state'—the translation of one crystal lattice against the other, and (ii) one parameter to indicate the position of the interface (required if the basis of either crystal structure includes more than one atom). The atomistic structure of an interface, however, not only involves the above crystallographic parameters; in all but the most trivial cases the atoms near the interface plane relax to positions that differ from those in their native crystal structure. Such relaxation may become apparent, for example, as misfit dislocation networks. Apart from being structural defects, internal interfaces often change the composition in the regions adjacent to the interface plane. This may have an eminent influence on materials properties. The conductivity of varistor ceramics, for example, sensitively depends on charged point defects that segregate to the grain boundaries and thus induce space charges in the adjacent crystallites.

In crystalline materials, one distinguishes between two different categories of internal interfaces: homophase boundaries and heterophase boundaries.[6] The former are commonly called grain boundaries, while the latter are often denoted as heterointerfaces. Grain boundaries include twin boundaries, domain boundaries, or inversion domain boundaries as special cases. Heterointerfaces, in contrast, separate crystallites of two thermodynamically different phases. The crystal structure and orientation of these two crystallites may be the same, as often desired in semiconductor heterostructures, or they may differ, as encountered, for example, at interfaces between tetragonal and monoclinic $ZrO_2$. Another important group are metal/ceramic interfaces, for which recent conference

*To whom correspondence should be addressed. Fax: +49-711-2095-320; e-mail: ruehle@herm.mpl-stuttgart.mpg.de

proceedings demonstrate considerable progress in the level of understanding.[3,7–9] For heterointerfaces, in contrast to grain boundaries, it is also important to understand their stability against chemical reactions and diffusion-related changes of their morphology.[10–12]

This paper reviews recent progress in determining the structure, composition, and interatomic bonding across interfaces by TEM and a few other experimental techniques. Shortly after first X-ray diffraction experiments had revealed that many inorganic materials are crystalline the question raised what the structure of the grain boundaries would be like. As one of the first theories, Rosenheim[13] envisioned grain boundaries as relatively thick, disordered regions of amorphous 'cement' between the crystallites. After the introduction of the concept of crystal dislocations, Taylor[14] correctly proposed a dislocation model for low-angle grain boundaries. For large-angle grain boundaries, however, the development of models has been much slower. Sutton and Vitek[15–17] were the first to show by computer simulation that large-angle grain boundaries are not amorphous but periodic and consist of unique structural units. Since then, advanced experimental and computation techniques have significantly advanced our understanding of the atomistic structure of grain boundaries as well as heterointerfaces.

## 2 Microstructure of Materials—TEM Studies of Interfaces

To rationalize the properties of polycrystalline materials one needs to quantify various parameters of their microstructure on different length scales. Light microscopy (LM) and—for features below 1 μm—scanning electron microscopy (SEM) constitute the major tools for such quantitative metallography. Concerning interfaces, it is important to investigate the frequency distribution of the misorientation between adjacent crystallites. The advent of 'orientation imaging microscopy' (OIM), automized evaluation of crystallite orientations from Kossel patterns obtained in an SEM, has now made it feasible to obtain this information with excellent statistics.[18,19] Still, this technique does not suffice to determine the interface inclination, which is equally important for the properties. OIM in combination with successive abrasion of the surface (depth profiling) may provide this information but is laborious, and the removal of very thin layers of material without introducing damage requires special experimental techniques.

TEM, in contrast to LM and SEM, can reveal the structure of interfaces and their composition down to atomic resolution. Table 1 compiles the most important TEM techniques for this purpose. Conventional TEM (CTEM) stands for imaging modes using only one beam—either the primary beam or one of the diffracted beams. CTEM imaging sensitively reveals strain fields around crystal defects. Besides imaging, CTEM includes (selected-area) diffraction studies with parallel illumination. This technique serves to analyze agglomerates of point defects, dislocations, and planar defects. It is well established that the microscopic defects observable by CTEM substantially influence macroscopic materials properties.[20]

**Table 1.** TEM methods

| | |
|---|---|
| CTEM | Conventional transmission electron microscope |
| STEM | Scanning transmission electron microscope |
| HRTEM | High-resolution transmission electron microscope |
| AEM | Analytical transmission electron microscope |
| XEDS | Energy-dispersive x-ray spectroscopy |
| EELS | Electron energy loss spectroscopy |
| ELNES | Electron loss near edge structure |

In contrast to CTEM, which exploits elastic electron scattering, analytical transmission electron microscopy (AEM)[21–24] relies on inelastic electron scattering, where an incident electron transfers part of its kinetic energy to the specimen. Most important for elemental analysis, the primary electron may ionize an atom in the specimen by knocking out some of its inner electrons. Two complimentary methods exist to utilize such inner shell ionization for chemical analysis, X-ray energy-dispersive spectroscopy (XEDS) and electron energy-loss spectroscopy (EELS). XEDS spectra reveal the elements present in the specimen by the characteristic X-rays the ionized atoms emit when an electron falls into an emptied state of an inner shell. EELS spectra provide equivalent information by indicating the characteristic energy losses of the primary electrons during inner-shell ionization.

Both, XEDS and EELS can provide quantitative information on the local composition. XEDS appears to be easier, however EELS offers a wealth of extra information.[24,25] In EELS spectra recorded with an energy resolution better than 1 eV the absorption edges exhibit a fine structure. The energy-loss near-edge structure (ELNES) dominates from the onset of the edge up to about 30 eV, whereas the 'extended' energy-loss fine structure (EXELFS) ranges from there up to several 100 eV above. ELNES studies can be used to determine the bonding, electronic structure, and real space structure around the atoms that lead to the respective absorption edge. ELNES features are generally complex and cannot be analyzed intuitively; the near-edge fine structure results from

multiple electron scattering and varies with the scattering atom, the number and species of the neighboring atoms, and the bond angles the scattering atom makes with its neighbors. The important point about ELNES is that it contains information about the three-dimensional atom arrangement around the scattering atom and, therefore, complements the results obtained by high-resolution transmission electron microscopy (HRTEM).[25]

As compared to SEM, performing AEM in a TEM allows one to obtain analytical data with high spatial resolution. The actual resolution depends on the size of the electron probe and beam broadening. In a dedicated scanning transmission electron microscope (STEM) the probe size is typically smaller than 1 nm, thus the lateral resolution can be less than 1 nm. Several different techniques of interface analysis have been developed in order to optimize the information content and time consumption under the given boundary conditions. The standard method consists of scanning the electron probe along a line across the interface while recording analytical signals.[26] This technique, however, substantially suffers from specimen drift. In many cases, the 'spatial difference technique' constitutes a better solution.[27,28] With that technique one scans the electron beam across three box-shaped regions of the same shape, one centered on the interface and the two others located in the two crystals next to the interface. The difference of the spectra obtained in these three regions then reveals the net effect of the interface. Further details of the AEM techniques applied to interfaces have been described by Dehm *et al.*[29]

To solve the atomistic structure of internal interfaces with high precision and in several crystallographic projections one needs to image the atom arrangement with a resolution of about 0·1 nm. Presently, high-resolution transmission electron microscopy (HRTEM) constitutes the most powerful technique for this purpose.[30] At the moment, two different kinds of HRTEM instruments achieve or closely approach the above resolution: High-voltage high-resolution transmission electron microscopes[31] and—a very recent development—medium voltage transmission electron microscopes equipped with a corrector to eliminate spherical aberration.[32,33] Owing to the coherent imaging process, intuitive interpretation of HRTEM images showing interface structures may lead to severe errors.[34] Dynamical electron diffraction in the specimen, aberrations of the electron optics, and loss of electron wave phase information generally lead to a complex relationship between the image and the atom arrangement in the specimen. One well-established method to correctly interpret HRTEM images relies on numerically simulating the images that hypothetical object structures would yield under the experimental imaging conditions. The simulated image that yields the best match with the experimental image under consideration identifies the best model for the real structure. This method has been automated to perform a structure refinement by 'iterative digital image matching'.[35–40]

## 3 Structure of Domain Boundaries in $PbTiO_3$ Ferroelectric Thin Films

Thin films of $PbTiO_3$ (lead titanate) have important device applications because this material is ferroelectric at room temperature. Above the Curie temperature $T_c \approx 400°C$ the material adopts the perovskite structure with the space group $Pm\bar{3}m$ (primitive cubic). On cooling below $T_c$ the symmetry reduces to $P4mm$ (tetragonal) with $c/a = 1{\cdot}09$ in a first order phase transition, during which the O and Ti ions move versus the Pb ions. The displacements occur along one of the six $<001>_c$ directions of the cubic cell. This particular axis then becomes the $c$ axis or $[001]_t$ direction of the tetragonal cell. The ion displacements destroy the inversion symmetry of the cubic structure; the material becomes polar and develops a spontaneous electrical polarization along $[001]_t$.

The $PbTiO_3$ films we discuss in the following have been grown on (001) MgO substrates at temperatures above $T_c$.[41] The films grow as a cubic single crystal, which then transforms to tetragonal $PbTiO_3$ on cooling to room temperature. The transformation does not leave behind a single crystal but a polycrystal consisting of *domains*, in which $[001]_t$ points into one of the six different $<100>_c$ directions. The domains meet in 'special' grain boundaries, denoted as *domain boundaries*. Conventional TEM has revealed that if the polarization vectors of the adjoining grains make an angle of 90°, the domain walls tend to lie parallel to $\{101\}_t$ planes. The energy and mobility of such 90° domain boundaries influence the technically important 'switching' behavior of the film—the response to external electric fields.

Both, the energy and mobility of a domain boundary depend on its width $w$. To advance the understanding of ferroelectric thin films, therefore, it is important to measure the domain width $w$. Figure 1 presents a HRTEM image of a 90° domain boundary in $[010]_t$ projection. However, it seems impossible to determine the boundary width $w$ by mere visual inspection of this image. Quantitative HRTEM, in contrast, allows to determine $w$ with high accuracy: After obtaining the electron intensity

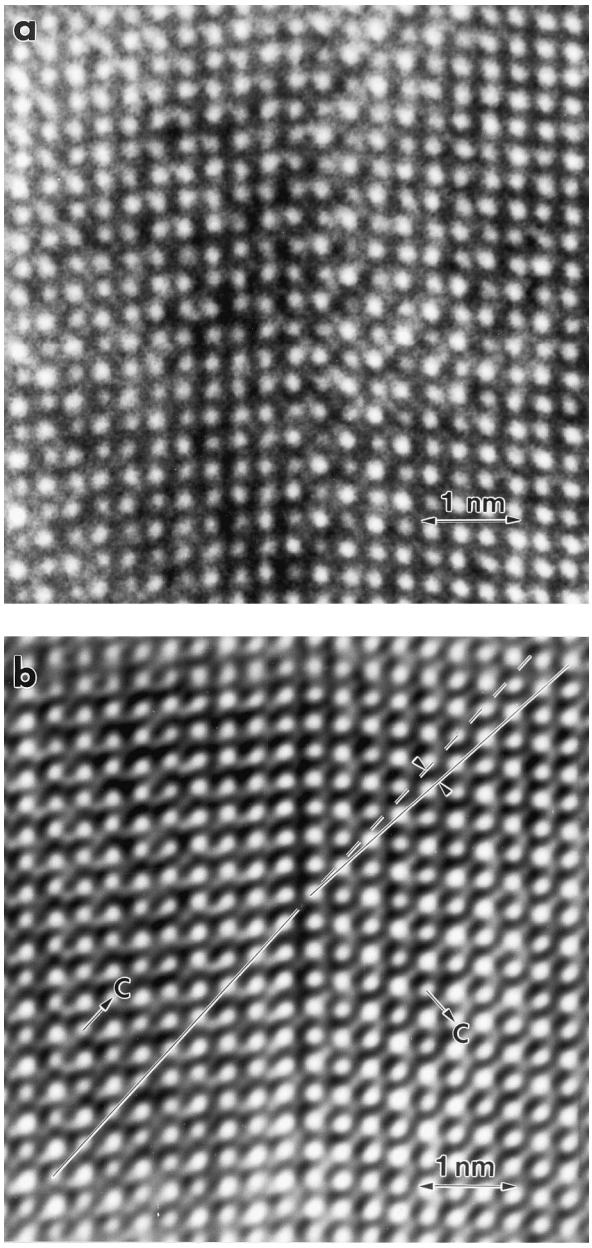


**Fig. 1.** (a) Experimental HRTEM image of a 90° domain boundary in $PbTiO_3$. The viewing direction coincides with the common *a* direction of the two grains. The boundary plane lies vertical in this image and corresponds to {101} on both sides. (b) The image after adaptive Fourier filtering. The angle between *c* on one side and *a* (or *b*) on the other side reflects the tetragonality of the low-temperature structure: $c/a = 1{\cdot}09$.

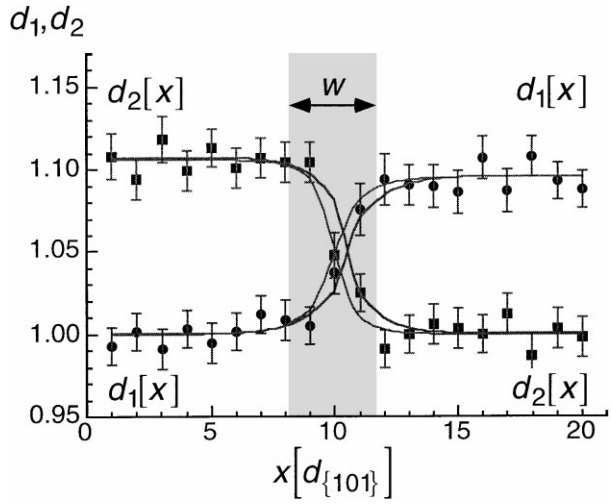


**Fig. 2.** Lattice parameters *a* and *c* across the domain boundary of Fig. 1, plotted versus the spatial coordinate normal to the boundary plane in units of the {101} spacing (0·29 nm). On the left, *a* and *c* correspond to $d_1$ and $d_2$, respectively, while on the right the meaning of $d_1$ and $d_2$ are interchanged. The width *w* of the domain boundary amounts to $(1{\cdot}0 \pm 0{\cdot}3)$ nm.

of the image in digital representation, the noise in the image was reduced by adaptive Fourier filtering.[42] From the resulting image the positions of Pb columns were extracted by cross-correlating the image with the pattern that each Pb column yields in simulated images of undisturbed $PbTiO_3$. The maxima of the cross-correlation image reveal where the pattern occurs in the image. By identifying the sites of maximum pattern similarity with the positions of Pb columns, and averaging over the positions parallel to the boundary plane a model was obtained for the repeat unit of the boundary structure. Figure 2 depicts the course of the lattice parameters $d_1$ and $d_2$ in this model.

So far, the analysis has not accounted for potential artefacts in the HRTEM image: owing to the problems outlined above, the coincidence between the position of Pb columns and the pattern of Pb columns in *undisturbed* $PbTiO_3$ may be destroyed near the domain boundary. To estimate the error arising from this problem, image simulations were carried out with those column positions obtained by the above procedure. The simulated image was analyzed in the *same* way as the experimental image 1. The difference between corresponding positions of Pb columns indicates the error originating from the disturbance of the column/pattern coincidence. The analysis has revealed that artefacts in the HRTEM image introduce errors no larger than 0·8% in the lattice parameters $d_1$ and $d_2$. Combining these errors with the standard error of the mean value of $d_1$ and $d_2$ along the boundary one obtains the error bars in Fig. 2.

Fitting a tanh function[43] to the data of Fig. 2 one obtains $w = (1{\cdot}0 \pm 0{\cdot}3)$ nm. The error of $\pm 0{\cdot}3$ nm results from the ambiguity in defining the exact location of the boundary plane (the fourth microscopic degree of freedom, compare Section 1), rather than from uncertainty in Pb column positions. The two solid curves in Fig. 2 result from fitting the data with a {202} boundary plane occupied by Pb–Ti–O or O, respectively. Inserting the result for *w* into the expression for the boundary energy in the theory of Cao and Cross[43] yields a boundary energy of $50\,\mathrm{mm}^{-2}$.

## 4 Structural and Compositional Studies of Grain Boundaries in $Si_3N_4$

$Si_3N_4$ (silicon nitride) ceramics are important structural materials for high-temperature applications. Owing to the covalent bonding, sintering of $Si_3N_4$ requires the addition of sintering aids. The latter oxidize the $Si_3N_4$ grains from the surface to form $SiO_2$, which covers the $Si_3N_4$ grains as a liquid phase before densification; $Si_3N_4$ can only be densified if a liquid phase is present. Kleebe *et al.*[44] showed that an amorphous film exists in all 'random' grain boundaries—boundaries without 'special' crystallography. The film thickness depends primarily on the composition of the film and is constant throughout a specific material. Clarke[45,46] suggested that the amorphous wetting film forms if the energy of the interfaces the two $Si_3N_4$ crystals make with the film is smaller than the (hypothetical) energy $\gamma_c$ of an unwetted grain boundary (Fig. 3). In agreement with this model, small-angle grain boundaries and 'special' grain boundaries[47] do not exhibit an amorphous film.

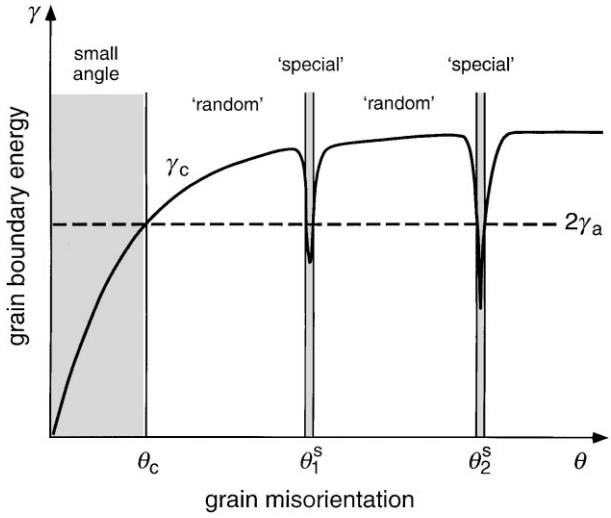


**Fig. 3.** Grain boundary energy $\gamma$ of two $Si_3N_4$ crystals versus the misorientation angle $\theta$ around a particular rotation axis [uvw] (schematic). Solid line: $\gamma_c$, *without* amorphous wetting layer. Dashed line: energy 2, $\gamma_a$ of a grain boundary containing an amorphous wetting layer (each solid/liquid interface contributes $\gamma_a$); this energy does not depend on θ. An amorphous film is expected to form where $2\gamma_a$ is smaller than $\gamma_c$.

Tanaka *et al.*[48] investigated the wetting film thickness as a function of the wetting film composition. Those studies revealed that an amorphous film exists on all large-angle grain boundaries, but the thickness depends on the sintering additives. In pure $Si_3N_4$ the $SiO_2$ wetting film has an equilibrium thickness of 1 nm. Small additions of CaO reduce the film thickness, while with increasing amounts of sintering additives the thickness increases—at least for non-special grain boundaries (Figs 4 and 5). According to the present understanding, the equilibrium thickness results from the balance of the following forces across the grain boundary: (i) attractive van der Waals forces and (ii) repulsive forces resulting from steric effects, and (iii) electric double-layer forces.[45,46,49] Different types of impurities

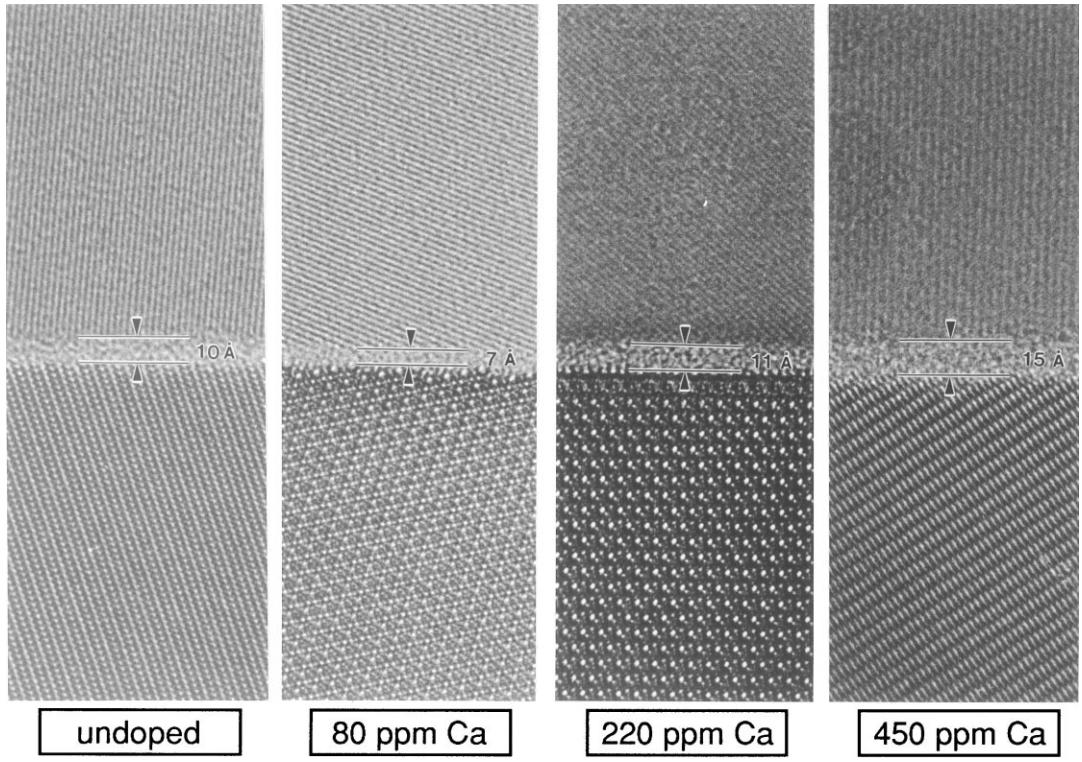


**Fig. 4.** HRTEM images revealing the dependence of the $SiO_2$ wetting layer thickness in $Si_3N_4$ grain boundaries on the amount of Ca sintering aid. (a) 0 ppm Ca, (b) 80 ppm Ca, (c) 220 ppm Ca, (d) 450 ppm Ca.

result in different equilibrium thicknesses. However, different amounts of impurities still result in the same equilibrium thickness of grain boundary film; increasing the impurity content merely increases the volume of triple junctions.

## 5 Structure and Composition of Grain Boundaries in $SrTiO_3$

The electrical properties of $SrTiO_3$ (strontium titanate) ceramics are strongly influenced or even dictated by grain boundary segregation of charged point defects, such as dopant atoms, impurities, vacancies, or self-interstitials. The atomistic structure of the grain boundaries, their energy, and the segregation of point defects mutually depend on each other. Grain boundary segregation of charged point defects induces the formation of space charges in the adjoining crystals.[50–54] In order to investigate the relation between grain boundary structure and composition, grain boundaries in Fe-doped $SrTiO_3$ bicrystals and in $SrTiO_3$ ceramics were studied by HRTEM and by AEM with subnanometer resolution.

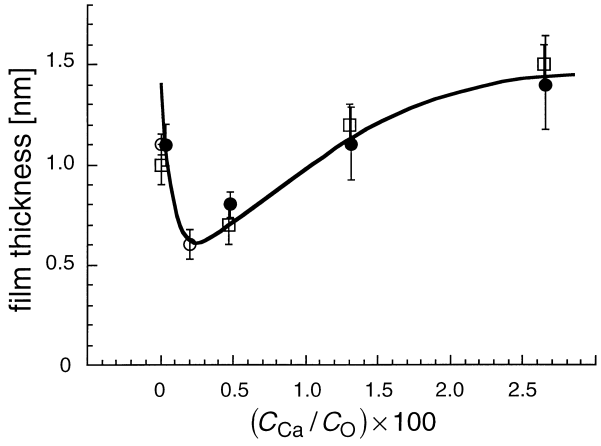


**Fig. 5.** $SiO_2$ wetting layer thickness in $Si_3N_4$ grain boundaries versus the Ca concentration.

### 5.1 Structure of 'special' grain boundaries

Quantitative HRTEM served to investigate the atomistic structure of $\sum=3$, (111) grain boundaries in Fe-doped $SrTiO_3$ bicrystals with a doping level of Fe/Ti = 0·04 at%.[38,55,56] Analysis of the translation state revealed that the $\sum=3$, (111) grain boundary has an excess volume: normal to the boundary plane, the spacing between the two crystals exceeds what one would expect from the crystallography by (0·06 ± 0·01) nm. AEM revealed no segregation of Fe above the present detection limit, which corresponds to 0·15 atoms/nm$^{-2}$.

The atomistic structure of $\sum=5$, (310) grain boundaries was also investigated by HRTEM studies on bicrystals, however only semi-quantitatively. Those bicrystals had an Fe doping level corresponding to Fe/Ti = 0·01 at%. Again, segregation of Fe to the grain boundary did not exceed the detection limit of AEM. By straight-forward interpretation of Z-contrast images, Browning and Pennycook have suggested a model for the atom configuration at this boundary.[57] Quantitative

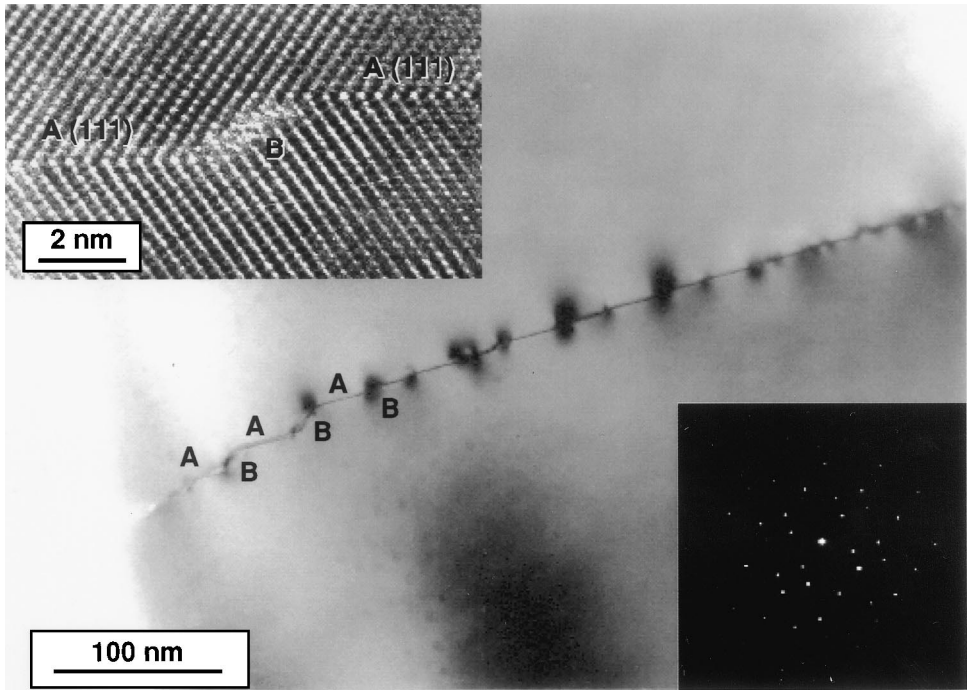


**Fig. 6.** $\sum=3$ grain boundary in polycrystalline $SrTiO_3$. On a macroscopic scale, the mean orientation of the boundary plane deviates by 4° from the orientation of {111} planes of the two crystals. On the microscopic scale, however, the grain boundary decomposes into two types of facets, *A* and *B*. Facets of type *A* correspond to {111} planes in both crystals, while facets of type *B* follow another, presumably 'random' plane.

HRTEM analysis of the grain boundary structure and, in particular, of the excess volume has not yet been carried out.

### 5.2 Grain boundaries in $SrTiO_3$ ceramics

In addition to the above 'special' grain boundaries in bicrystals, 'non-special' or 'random' grain boundaries were investigated in $SrTiO_3$ ceramics with an Fe doping level corresponding to Fe/Ti = 0·4 at%. It was found that this material actually contains a high density of $\sum = 3$ grain boundaries. One example for these boundaries is shown in Fig. 6. The mean orientation of the boundary plane deviates from {111} planes in the two grains. The TEM image reveals that the grain boundary decomposes into two types of facets, *A* and *B*. Facets of type *A* correspond to {111} planes in both crystals and exhibited similar features as described for $\sum = 3$, (111) bicrystals in Section 5.1. At this type of facet the Fe segregation was below the detection limit. Facets of type *B*, in contrast, have a 'non-special' ('random') orientation. These facets are inclined versus the viewing direction. The 0·3 nm broad band of diffuse contrast in the boundary region suggests that facet contains an amorphous film. For facets of type *B*, AEM indicated Fe segregation corresponding to 0·46 atoms $nm^{-2}$.

In completely 'random' grain boundaries of the same material HRTEM revealed the existence of an amorphous film with a thickness of 0·8 nm (Fig. 7). Moreover, the segregation of Fe was much stronger than in the $\sum = 3$ boundaries: 4·0 atoms $nm^{-2}$ along with a Ti excess of 8·5 atoms $nm^{-2}$. These results have a similar interpretation as given above for $Si_3N_4$ ceramics: 'Special' grain boundaries with an energy below 2 $\gamma_a$, (2 times the energy $\gamma_a$ of a crystalline/ amorphous interface) have no amorphous film, and cause no segregation of cations (also see Fig. 3). 'Non-special' boundaries, on the other hand, contain an amorphous film with a thickness of about 0·8 nm, which forms because without the film the energy of the grain boundary would exceed 2 $\gamma_a$. Table 2 summarizes the results that have been obtained so far for different grain boundaries in $SrTiO_3$.

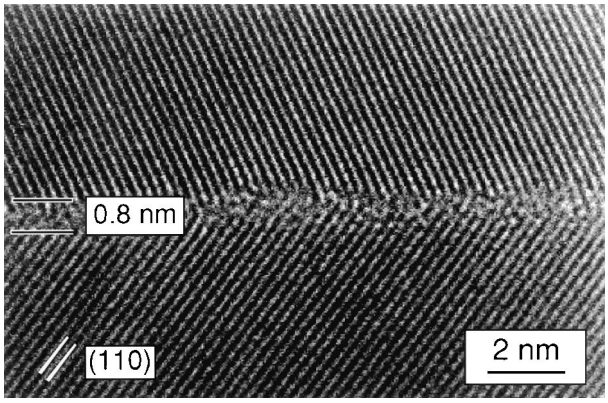


**Fig. 7.** HRTEM image of a 'random' grain boundary in polycrystalline $SrTiO_3$ (same material as in Fig. 6), revealing an amorphous film between the two crystals.

**Table 2.** Properties of different grain boundaries in $SrTiO_3$

| *Sample* | *Fe doping* $C_{Fe}/C_{Ti}$ | *Fe excess* $\theta_{Fe}$ | *Notes* |
|---|---|---|---|
| | Bicrystals | | |
| $\sum = 3$, (111) (Verneuil method) | 0·04 at% | < detection limit | |
| $\sum = 5$, (310) (diffusion bonded) | 0·01 at% | < detection limit | |
| near $\sum = 13$, (510) (diffusion bonded) | 0·47 at% | (0·46 ± 0·13) atoms $nm^{-2}$ | |
| | Polycrystal | | |
| near $\sum = 3$, (111) | 0·40 at% | | |
| (111) facets | | < detection limit | |
| 'random' facets | | (0·46 ± 0·13) atoms $nm^{-2}$ | |
| 'random'boundary | 0·40 at% | (4·0 ± 0·26) atoms $nm^{-2}$ | Amorphous film (0·8 nm); Ti excess (8·5 ± 1·6) atoms $nm^{-2}$ |

## 6 Summary and Conclusion

TEM constitutes a particularly powerful experimental technique to study grain boundaries in ceramics. Through the newly developed methods of quantitative HRTEM it has become possible to determine the atom positions at grain boundaries with high precision—even though this method works only for grain boundaries where the misorientation of the two grains has pure tilt character (no twist component). The accuracy of structure determination depends not only on the resolution limit of the electron microscope, but also on the quality of the TEM specimen (thickness, contamination layers, and the like). Analytical TEM, on the other hand, provides highly resolved information on the spatial distribution of atomic species at interfaces. Here the limit of delectability depends not only on the instrumentation but also on the type of elements under investigation. Instrumental developments in the near future will allow analysis of the fine structure in EELS spectra with much better energy resolution, and such analysis will yield very detailed information on the nature of interatomic bonds across interfaces.

Even though TEM offers many advantages for the study of grain boundaries, such studies are particularly time-consuming. Moreover, the volume one can image or analyze by TEM is extremely small. Usually, therefore, it is not trivial

to conclude from TEM observations on the average or macroscopic properties of materials.

## References


1. Wolf, D. and Yip, S. (eds), *Materials Interfaces*. Chapman and Hall, London, 1992.
2. Sutton, A. P. and Balluffi, R. W., *Interfaces in Crystalline Materials*. Clarendon Press, Oxford, 1996.
3. Rühle, M., Balluffi, R. W., Fischmeister, H. F. and Sass, S. L. (eds), *Journal de Physique C4* 1985, **46**.
4. Ferro, A. C, Conde, E. P. and Fortes, E. A. (eds), *Intergranular and Interphase Boundaries in Materials*. Trans Tech Publications, Zürich, 1996.
5. Gleiter, H., Nanocrystalline materials. *Progress Mat. Sci.*, 1989, **33**, 223–315.
6. Kalonji, G. and Cahn, J. W., Symmetry constraints on the orientation dependence of interfacial properties. The group of the Wulff plot. *Journal de Physique C6*, 1982, **43**, 25–31.
7. Rühle, M., Heuer, A. H., Evans, A. G. and Ashby, M. F. (eds), *Acta Metallurgica et Materialia*, 1992, **S40**.
8. Rühle, M., Evans, A. G., Ashby, M. F. and Hirth, J. P. (eds), *Metal–Ceramic Interfaces*. Pergamon Press, Oxford, 1990.
9. Rühle, M. and Mader, W., Heterophase boundaries. In *Designing Interfaces for Technological Applications* ed S. D. Peteves. Elsevier Applied Science, London, 1989, pp. 145–195.
10. Backhaus-Ricoult, M., Diffusion processes and interphase boundary morphology in ternary metal–ceramic systems. *Ber. Bunsenges. Phys. Chem.*, 1986, **90**, 684–690.
11. Schmalzried, H., Solid state reactions and the role of phase boundaries. *Polish Journal of Chemistry*, 1993, **67**, 167–190.
12. Schmalzried, H. and Backhaus-Ricoult, M., Internal solid state reactions. *Progr. Solid State Chem.*, 1994, **22**, 1–58.
13. Rosenheim, W. *J. Inst. Metals*, 1912, **8**, 149–173.
14. Taylor, G. I., *Proc. Roy. Soc. A*, 1934, **145**, 362.
15. Sutton, A. P. and Vitek, V., On the structure of tilt grain boundaries in cubic metals. I. Symmetrical tilt boundaries. *Philosophical Transactions of the Royal Society of London A*, 1983, **309**, 1–36.
16. Sutton, A. P. and Vitek, V., On the structure of tilt grain boundaries in cubic metals. II. Asymmetrical tilt boundaries. *Philosophical Transactions of the Royal Society of London A*, 1983, **309**, 37–54.
17. Sutton, A. P. and Vitek, V., On the structure of tilt grain boundaries in cubic metals. III. Generalizations of the structural study and implications for the properties of grain boundaries. *Philosophical Transactions of the Royal Society of London A*, 1983, **309**, 55–68.
18. Adams, B. L., Orientation imaging: the emergence of a new microscopy. *Met. Trans. A*, 1993, 819–831.
19. Dingley, D., Automated materials characterization in electron microscopy. In *Electron Microscopy 1998*, ed. H. A. C. Benavides and M. J. Yacarnan. Institute of Physics Publishing, Bristol, 1998, pp. 29–31.
20. Hirsch, P. B., Howie, A., Nicholson, R. B., Pashley, D. W. and Whelan, M. J., *Electron Microscopy of Thin Crystals*. Butterworths, London, 1965.
21. Hren, J. J., Goldstein, J. I. and Joy, D. C. (eds), *Introduction to Analytical Electron Microscopy*. Plenum Press, New York, 1979.
22. Williams, D. B. and Carter, C. B., *Transmission Electron Microscopy*. Plenum Press, New York, 1996.
23. Williams, D. B., *Practical Analytical Electron Microscopy in Materials Science*. Verlag Chemie, Weinheim, 1984.
24. Egerton, R. F., *Electron Energy-loss Spectroscopy in the Electron Microscope*. Plenum Press, New York, 1986.
25. Krivanek, O. L. (ed.), *Microscopy and Microanalysis of Microstructures*, 1995, **6**, 1–157.
26. Duscher, C., Browning, N. D. and Pennycook, S. J., Atomic column resolved electron energy-loss spectroscopy. *Phys. Stat. Sol. (a)*, 1998, **166**, 327–342.
27. Gu, H., Ceh, M., Stemmer, S., Mullejans, H. and Rühle, M., A quantitative approach for spatially resolved electron energy-loss spectroscopy of grain boundaries planar defects on a subnanometer scale. *Ultramicroscopy*, 1995, **59**, 215–227.
28. Müllejans, H. and Bruley, J., Electron energy-loss spectroscopy (EELS): comparison with x-ray analysis. *Journal de Physique C7*, 1993, **3**, 2083–2092.
29. Dehm, G., Ernst, F., Mayer, J., Möbus, G., Mülejans, H., Phillipp, F., Scheu, C. and Rühle, M., Transmission electron microscopy at the Max-Planck-Institut ffir Metallforschung. *Z. MetalIkde.*, 1996, **87**, 898–910.
30. Ernst, F. and Rüle, M., Present developments in high-resolution transmission electron microscopy. *Current Opinion in Solid State and Materials Science*, 1997, **2**, 469–476.
31. Phillipp, R, Möbus, G. and Rüle, M., New high-voltage atomic resolution microscope approaching 1 Å point resolution installed in Stuttgart. *Ultramicroscopy*, 1994, **56**, 1–10.
32. Haider, M., Braunshausen, G. and Schwan, L., Correction of the spherical aberration of a 200 kV TEM by means of a hexapole-corrector. *Optik*, 1995, **99**, 167–179.
33. Kabius, B., Urban, K., Haider, M., Uhlemann, S., Schwarz, E. and Rose, H., First applications of a spherical-aberration corrected transmission electron microscope in materials science. In *Electron Microscopy 1998*, ed. H. A. C. Benavides and M. J. Yacaman. Institute of Physics Publishing, Bristol, 1998, pp. 609–610.
34. Spence, J. C. H., *Experimental High-resolution Electron Microscopy*. Clarendon Press, Oxford, 1980.
35. Ernst, F., Hofmann, D., Nadarzinski, K., Stemmer, S. and Streiffer, S. K., Quantitative high-resolution electron microscopy of interfaces. In *Intergranular and Interphase Boundaries in Materials*, ed. A. C. Ferro, E. P. Conde and E. A. Fortes. Trans Tech Publications, Zürich, 1996, pp. 23–34.
36. Hofmann, D. and Ernst, F., Quantitative HRTEM of the Incoherent Twin Boundary in Cu. *Ultramicroscopy*, 1994, **53**, 205–221.
37. Nadarzinski, K. and Ernst, F., The atomistic structure of a $\sum = 3$, (111) grain boundary in NiAl, studied by quantitative high-resolution transmission electron microscopy. *Phil. Mag. A*, 1996, **74**, 641–664.
38. Kienzle, O, Exner, M. and Ernst, R., Atomistic structure of the $\sum = 3$, (111) grain boundary in strontium titanate. *Phys. Stat. Sol. (a)*, 1998, **166**, 57–71.
39. Möbus, G., Retrieval of crystal defect structures from HREM images by simulated evolution. I. Basic technique. *Ultramicroscopy*, 1996, **65**, 205–216.
40. Möbus, G. and Dehm, G., Retrieval of crystal defect structures from HREM images by simulated evolution. II. Experimental image evaluation. *Ultramicroscopy*, 1996, **65**, 217–228.
41. Hsu W.-Y., Growth, domain structures, and nonlinear optical properties of ferroelectric lead titanate thin films. Thesis, Comell University, 1994.
42. Möbus, G., Necker, G. and Rühle, M., Adaptive Fourier-filtering technique for quantitative evaluation of high-resolution electron micrographs of interfaces. *Ultramicroscopy*, 1993, **49**, 46.
43. Cao, W. and Cross, L. E., Theory of tetragonal twin structure in ferroelectric perovskites with a first-order phase transition. *Phys. Rev. B*, 1991, **44**, 5–12.
44. Kleebe, H. J., Cinibulk, M. K., Cannon, R. M. and Rühle, M., Statistical analysis of the intergranular film thickness in silicon nitride ceramics. *J. Am. Ceram. Soc.*, 1993, **76**, 1969–1977.
45. Clarke, D. R., Grain boundaries in polyphase ceramics. *Journal de Physique C4*, 1985, **46**, 51–59.

46. Clarke, D. R., On the equilibrium thickness of intergranular glass phases in ceramic materials. *J. Am. Ceram. Soc.*, 1987, **70**, 15–22.
47. Gleiter, H. and Chalmers, B., *High Angle Grain Boundaries*. Pergamon press, Oxford, 1972.
48. Tanaka, L, Kleebe, H. J. and Cinibulk, M. K., Calcium concentration dependence of the intergranularfilm thickness in silicon nitride. *J. Am. Ceram. Soc.*, 1994, **77**, 911–914.
49. Clarke, D. R., Possible electrical double-layer contribution to the equilibrium thickness of intergranular glass films in polycrystalline ceramics. *J. Am. Ceram. Soc.*, 1993, **76**, 1201–1204.
50. Maier, J., Defect chemistry in heterogeneous systems. *Solid State Ionics*, 1995, **75**, 139–145.
51. Chiang, Y. M. and Takagi, T., Grain-boundary chemistry of barium titanate and strontium titanate: II, origin of electrical barriers in positive-temperature-coefficient thermistors. *J. Am. Ceram. Soc.*, 1990, **73**, 3286–3291.
52. Chiang, Y. M. and Takagi, T., Grain-boundary chemistry of barium titanate and strontium titanate: I, high-temperature equilibrium space charge. *J. Am. Ceram. Soc.*, 1990, **73**, 3278–3285.
53. Desu, S. B. and Payne, D. A., Interfacial segregation in perovskites: I, theory. *J. Am. Ceram. Soc.*, 73, **90**, 3391–3397.
54. Desu, S. B. and Payne, D. A., Interfacial segregation in perovskites: II, experimental evidence. *J. Am. Ceram. Soc.*, 1990, **73**, 3398–3406.
55. Kienzle, O., Ernst, F. and Möbus, G., Confidence levels for structure retrieval of a ternary system. *Journal of Microscopy*, 1998, **190**, 144–158.
56. Kienzle, O. and Ernst, F., Effect of shear stress on the atomistic structure of a grain boundary in strontium titanate. *J. Am. Ceram. Soc.*, 1997, **80**, 1639–1644.
57. Browning, N. D. and Pennycook, S. J., Direct experimental determination of the atomic structure at internal interfaces. *Journal of Physics D*, 1996, **29**, 1779–1798.